



Cite this: *Nanoscale*, 2019, **11**, 5693

Nanotopography-based engineering of retroviral DNA integration patterns†

Yoon-ha Jang,^{‡a} Yi-seul Park,^{‡b} Jung-soo Nam,^c Yeji Yang,^a Ji-eun Lee,^a Kwang-hee Lee,^d Minho Kang,^e Alex Chialastri,^{ID f} Hohsuk Noh,^g Jungwon Park,^{e,h} Jin Seok Lee^{ID *b} and Kwang-il Lim^{ID *a,c}

Controlling the interactions between cells and viruses is critical for treating infected patients, preventing viral infections, and improving virus-based therapeutics. Chemical methods using small molecules and biological methods using proteins and nucleic acids are employed for achieving this control, albeit with limitations. We found, for the first time, that retroviral DNA integration patterns in the human genome, the result of complicated interactions between cells and viruses, can be engineered by adapting cells to the defined nanotopography of silica bead monolayers. Compared with cells on a flat glass surface, cells on beads with the highest curvature harbored retroviral DNAs at genomic sites near transcriptional start sites and CpG islands during infections at more than 50% higher frequencies. Furthermore, cells on the same type of bead layers contained retroviral DNAs in the genomic regions near cis-regulatory elements at frequencies that were 2.6-fold higher than that of cells on flat glass surfaces. Systems-level genetic network analysis showed that for cells on nanobeads with the highest curvature, the genes that would be affected by cis-regulatory elements near the retroviral integration sites perform biological functions related to chromatin structure and antiviral activities. Our unexpected observations suggest that novel engineering approaches based on materials with specific nanotopography can improve control over viral events.

Received 29th August 2018,
Accepted 4th March 2019

DOI: 10.1039/c8nr07029f

rscl.li/nanoscale

Introduction

Cells in an animal body react to various external cues from the environment, which may be physical, chemical, biological, or a combination thereof at the molecular level.^{1–4} Multiple types of cues are often concurrently transferred to target cells in the context of cellular interactions with substrates, neighboring cells, moving immune cells, and even invading foreign

biological entities. Before completely understanding the mechanisms involved in these complicated interactions, proactive engineering of a single cue may prompt cells respond to other concurrent cues in ways desired for biomedical applications.

The physical properties of engineered nanomaterials render them suitable candidates as environmental cues for controlling the overall cellular responses to external biological stimulants. Their dimension, from a few to hundreds of nanometers, coincides with the sizes of proteins and molecular domain structures, such as lipid rafts⁵ on the cell surface, which favors the development of effective interactions with cells. In addition, the morphological and biochemical behaviors of cells, although partially determined by their genetic programs, are also strongly affected by the matrix onto which cells are grown.⁶ This supporting matrix can be easily constructed to possess pre-designed structures in terms of dimensions of cells or subcellular parts by chemically synthesizing, assembling, and conjugating nanomaterials.^{7,8}

Gene delivery *via* viral infections is a medically important example where cellular responses to external cues (here viruses as invading foreign entities) have to be controlled with sophistication. In particular, retroviruses have been most frequently utilized as gene delivery vectors in gene and cell therapy because of their ability to integrate transgenes into the host

^aDepartment of Chemical and Biological Engineering, Sookmyung Women's University, Seoul, 04310, South Korea. E-mail: klim@sookmyung.ac.kr

^bDepartment of Chemistry, Sookmyung Women's University, Seoul 04310, South Korea. E-mail: jinslee@sookmyung.ac.kr

^cDepartment of Medical and Pharmaceutical Sciences, Sookmyung Women's University, Seoul, 04310, South Korea

^dM monitor, Inc., Daegu, 42713, South Korea

^eCenter for Nanoparticle Research, Institute for Basic Science (IBS), Seoul 08826, South Korea

^fDepartment of Chemical Engineering, University of California at Santa Barbara, Santa Barbara, CA 93106-5080, USA

^gDepartment of Statistics, Sookmyung Women's University, Seoul, 04310, South Korea

^hSchool of Chemical and Biological Engineering, Institute of Chemical Process, Seoul National University, Seoul 08826, South Korea

†Electronic supplementary information (ESI) available. See DOI: 10.1039/c8nr07029f

‡These authors contributed equally.

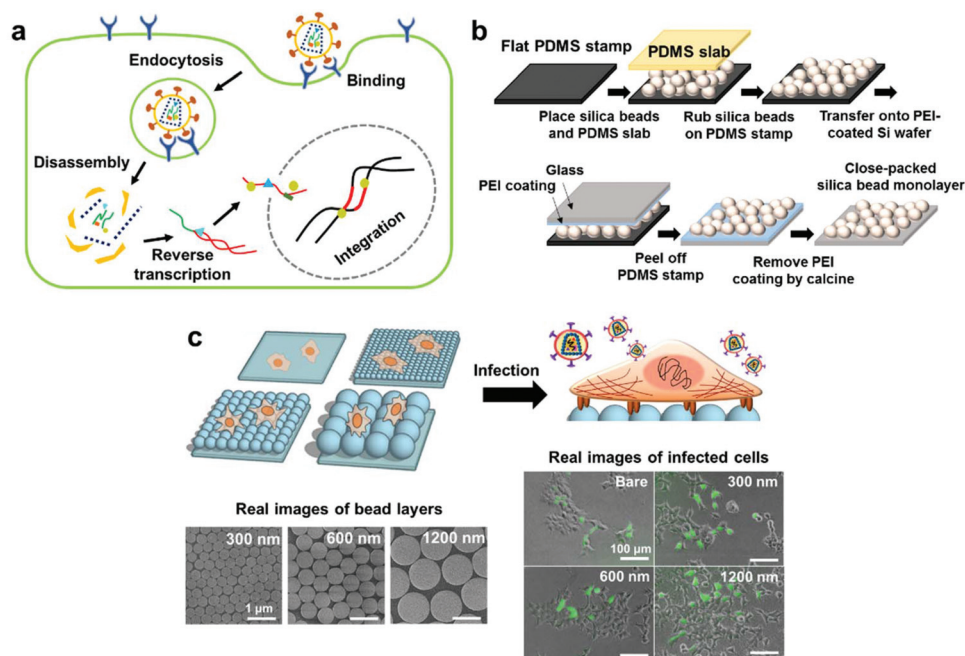


Fig. 1 Infection of cells on engineered nanobead layers. (a) A brief summary of retroviral infection steps. (b) Fabrication steps for close-packed silica nanobead monolayers. (c) Schematic illustrations for culture of human cells on flat glass and nanoscale bead layers and retroviral infections of the cells. In addition, scanning electron microscopy (SEM) images of nanobead monolayers are shown (scale bars are 1 μm). Epifluorescence images of infected HEK 293T cells are also shown (scale bars are 100 μm). Some cells showed green fluorescence because of the expression of eGFP from the corresponding gene delivered by retroviral vector.

genome.^{9–11} Retroviral vectors gain entry into cells *via* binding of viral envelope proteins to cellular surface proteins (Fig. 1a). The bound retroviral vector particles are often internalized *via* endosomes (for example, when pseudotyped with vesicular stomatitis virus G (VSVG) protein) and then disassembled in the cytoplasm of host cells. Subsequently, the viral RNA genome is converted to double-stranded DNA by the viral reverse transcriptase and finally integrated into host chromosomes in the nucleus by viral integrase (Fig. 1a).

The patterned spatial distribution of the integrated DNAs in the host genome, with preference for some functional genomic domains, marks cellular response to retroviruses or interactions with these nanoscale invaders. Highly advanced retroviral vectors for therapeutic purposes and retrovirus-based molecular tools capable of modifying the human genome for genetic studies can be developed if retroviral integration patterns can be effectively altered or tuned.

We speculated that the mechanism by which cells respond to one type of environmental cue may affect the response to other types of concurrent cues. Based on this hypothesis, we attempted to alter retroviral integration patterns as a result of the response of human cells to retroviral invasion by prompting cells to react to characteristic nanoscale topography of substrates as an environmental cue.

Our observations showed that retroviral integrations can be sharply shifted toward regulatory genomic domains by growing cells in a special environment that included the curved surface of silica bead layers. This highlights the poten-

tial of the nanotopography of engineered substrates for manipulating the interactions between cells and viruses.

Experimental

Synthesis of silica beads

Silica nanobeads were prepared using two methods according to their size. Beads with diameter of 300 or 600 nm were synthesized using the Stöber method. Tetraethyl orthosilicate (TEOS; Sigma-Aldrich, St Louis, MO, USA) was added to a solution consisting of ethanol (Samchun Pure Chemical, Seoul, Korea), 28% ammonium hydroxide (NH_4OH ; Samchun Pure Chemical), and distilled deionized water, and the solution was mixed by stirring for 3 h at room temperature. The 300 nm silica beads were prepared by adding 2 mL of TEOS to a solution consisting of 70 mL of ethanol, 2.7 mL of 28% NH_4OH , and 4.2 mL of distilled deionized water. For the preparation of 600 nm silica beads, 20 mL of TEOS, 350 mL of ethanol, 93.75 mL of 28% NH_4OH , and 2.6 mL of distilled deionized water were used. Silica nanobeads were formed by catalytic hydrolysis of TEOS with NH_4OH in the solution, where their diameter was controlled by varying the concentration and injection rates of the reactants. Larger silica beads with diameter of 1200 nm were synthesized using KCl (Samchun Pure Chemical) as an additive. For the synthesis of 1200 nm silica beads, 6.2 mg of KCl and 1.7 mL of 28% NH_4OH were dissolved in a mixture of distilled deionized water (2.9 mL) and

ethanol (20 mL) at 36 °C, followed by injection of a solution consisting of TEOS (1.5 mL) and ethanol (9 mL) at a rate of 0.1 mL min⁻¹. The mixture was stirred at 500 rpm for 5 h, and the formed silica beads were washed three times with ethanol and distilled deionized water in repeated centrifugation-ultrasonic dispersion cycles. The washed silica beads were resuspended in a small volume of ethanol and sonicated for 30 min to obtain a monodispersed solution. The silica beads in ethanol were transferred to a Petri dish and dried at room temperature, yielding spherical silica beads with various diameters, which were characterized using scanning electron microscopy (SEM).

Assembly of silica beads into a monolayer

The whole assembly process for silica bead monolayers is shown in Fig. 1b. Glass slides (Marienfeld-Superior, Lauda-Königshofen, Germany) were cut into 1 × 1 cm squares and then immersed in a Piranha solution composed of sulfuric acid (Samchun Pure Chemical) and hydrogen peroxide (Samchun Pure Chemical) at 3 : 1 volume/volume percentage ratio for over 30 min to remove surface oxides, followed by several rinses with distilled deionized water. The prepared glass substrates were plasma-treated for 10 min to create a hydrophilic surface, and then spin-coated with 30% (volume/volume) polyethyleneimine (PEI, $M_w = \sim 800$; Sigma-Aldrich) in distilled deionized water at 5000 rpm for 60 s. A small amount of dried silica bead powder was placed on flat polydimethylsiloxane stamps (PDMS; Dowhitech Silicone Co., Seoul, Korea) and then rubbed with the PDMS slab repeatedly until the silica beads were assembled as a monolayer. Silica bead monolayers were transferred to the PEI-coated glass substrate and the PEI coating was then removed by calcining in a furnace at 500 °C for 3 h. Silica bead monolayers on glass substrates were washed with distilled deionized water and dried under N₂ gas.

Cell culture and virus packaging

Human embryonic kidney (HEK) 293T cells (ATCC, Manassas, VA, USA) were cultured in Iscove's modified Dulbecco's medium (Life Technologies, Carlsbad, CA, USA) with 10% (volume/volume) fetal bovine serum (Gibco, Carlsbad, CA, USA) and 1% (weight/volume) penicillin/streptomycin (Gibco) at 37 °C and 5% CO₂. To produce pseudotyped murine leukemia virus (MLV)-based retroviral particles, plasmids encoding the viral genome (pCLPIT GFP, 10 µg), Gag-Pol polyproteins (pCMV gag-pol, 6 µg), and envelope proteins (pcDNA IVS VSVG, 4 µg) were introduced into 10 cm dishes of HEK 293T cells *via* a conventional method, calcium phosphate-based transfection. This method involves co-precipitation of calcium phosphate and DNA molecules, and both chemicals ultimately facilitate binding of DNA to the cell surfaces. The culture medium was changed at 12 h post-transfection. The cell supernatant containing viral particles was harvested twice at 36 h and 60 h post-transfection. The harvested supernatant was filtered through a 0.45 µm syringe filter, underlaid with a 20% (weight/volume) sucrose cushion, and concentrated by ultracentrifugation (Optima™ Ultracentrifuge LE-80 K, Beckman

Coulter, Brea, CA, USA) at 4 °C. The packaged retrovirus particles were resuspended with phosphate-buffered saline (PBS; Gibco).

Retroviral infection of cells

Before infection, HEK 293T cells were grown on bare glass (square shape, 0.25 inch × 0.25 inch) or two-dimensional (2D) arrays of silica beads of 300 nm, 600 nm, and 1200 nm diameters that were top-layered on bare glass. At 7 h post-growth, retrovirus particles in PBS were added to HEK 293T cells for infection.

Quantification of infected cells

The gene encoding enhanced green fluorescent protein (eGFP) was introduced into the viral genome to facilitate quantification of viral infection of cells.¹² At 4 days post-infection of HEK 293T cells, the fraction of eGFP-positive cells was quantified using the FACSCanto II flow cytometry system (BD Biosciences, San Jose, CA, USA).

Identifying cell and retrovirus genome junctions

After infection, the HEK 293T cells were further cultured for 8 days and host genomic DNA was isolated from the cells using the DNA mini kit (Qiagen, Hilden, Germany) to analyze the distribution of retroviral DNA integration sites in the host cell genome. The junctions of the 3' end of integrated retroviral genome and the adjacent host genomic DNA were specifically amplified using molecular biology techniques. First, the isolated host cell genomic DNA was fragmented by a restriction reaction with BamH I (New England Biolabs (NEB), Ipswich, MA, USA). Host cell and retrovirus genome junctions were selectively and linearly amplified by polymerase chain reaction (PCR) with a single 5' biotinylated DNA primer binding to a site within the 3' long terminal repeat (LTR) of the integrated retroviral genomic DNA and Taq DNA polymerase (NEB). The thermal cycle conditions for this PCR were as follows: initial denaturation at 95 °C for 5 min, 40 cycles of denaturation at 95 °C for 1 min, annealing at 55 °C for 45 s, and extension at 72 °C for 90 s. Additional extension at 72 °C for 10 min and cooling at 4 °C for 5 min were performed (C1000™ thermal cyclers, Bio-Rad, Hercules, CA, USA). Next, the single-stranded and biotinylated PCR products that contained the 3' end of integrated retroviral DNA and possibly the neighboring host genome junction DNA were selectively separated from the whole PCR reaction mixture using the Dynabeads® M-280 streptavidin system (Thermo Fisher Scientific, Waltham, MA, USA). These separated single-stranded DNA molecules were used as templates to synthesize their complementary DNA molecules (cDNA) *via* a reaction with random hexamers and Klenow enzymes (NEB). The synthesized double-stranded DNA molecules were cleaved with a single restriction enzyme, Mse I (NEB), as reported previously,^{13–18} and then ligated to linker DNA molecules using T4 DNA ligase (NEB). These linker DNA molecules were prepared by annealing two oligonucleotides (linker+: 5'-GTAATACGACTCACTATAGGGCTCCGCTTAAGG-GAC-3' and linker-: 5'-TAGTCCCTTAAGCGGAG-NH²-3'). The

linker-ligated DNA molecules were amplified *via* PCR with two primers binding to the 3' LTR of the integrated retroviral DNA and the linker DNA sequence (forward: 5'-biotin-GACTTG-TGGTCTCGCTGTTCCCTTGG-3' and reverse: 5'-GTAATACGACTC-ACTATAGGGCTCCGCTTAAG-3'). For this, PCR Phusion high-fidelity polymerase (NEB) was used, and the following thermal cycling conditions were applied: initial denaturation at 98 °C for 2 min, 25 cycles of denaturation at 98 °C for 2 min, annealing at 55 °C for 90 s, extension at 72 °C for 1 min, final additional extension at 72 °C for 5 min, and cooling at 10 °C for 3 min.

Next-generation sequencing of junction DNAs and mapping to the human genome

Two consecutive rounds of PCR were performed to add adaptor and index sequences to the ends of the amplified cell-virus genome junction DNA for downstream next-generation sequencing (NGS) analysis. These reactions were performed with Phusion high-fidelity polymerase (NEB) and primers (for adaptor addition, forward: 5'-TCGTCGGCAGCGTCAGATGTGTATAAGAGACAGGGAGGGTCTCCTCTGAGTGATTGACTACC-3' and reverse: 5'-GTCTCGTGGGCTCGGAGATGTGTATAAGAGACAGACTACTATAGGGCTCCGCTTAAGGAC-3'; for index addition, forward: 5'-AATGATACGGCGACCACCGAGATCTACACTCTCTATTTCGTCGGCAGCGTC-3' and reverse: 5'-CAAGCAG-AAGACGGCATAAGATNNNNNNNNGTCTCGTGGGCTCGG-3'). The actual indexing part in the reverse primer is denoted by "NNNNNNNN". Different thermal cycle conditions were applied for these two rounds of PCR. For adaptor addition, an initial denaturation step at 98 °C for 2 min was followed by 25 cycles of denaturation at 98 °C for 2 min, annealing and extension as a single step at 72 °C for 90 s, final additional extension at 72 °C for 5 min, and cooling at 10 °C for 3 min. For index addition, an initial denaturation step at 98 °C for 2 min was followed by 8 cycles of denaturation at 98 °C for 12 s, annealing and extension as a single step at 72 °C for 90 s, final additional extension at 72 °C for 5 min, and cooling at 10 °C for 3 min.

Sequencing using the Illumina MiSeq and raw read processing were performed by Macrogen Inc. (Seoul, Korea), a sequencing service provider. Raw reads with quality scores below 20 were filtered out with PRINSEQ-lite (version 0.20.4), and only cell-virus genome junction sequences that contained the end part of the retroviral 3' LTR (5'-GGAGGGTCTCCTCTGAGTGATTGACTACCGTCAGCGGGGTCTTTCA-3', 48 bp) were selected using the EMBOSS Needle (version 6.6.0.0) and in-house scripts with 2 bp mismatch allowance for downstream bioinformatics analysis. After removing all redundant sequences, the cell portions of the finally obtained cell-virus junction sequences were mapped to the human genome (GRCh37/HG19) using the QuickMap tool.¹⁹

Genetic network analysis

Genetic network analysis was performed for genes using the GeneMANIA.^{20,21} This tool generates several networks where genes, each as a node, are connected to other genes if they are functionally related, co-expressed, colocalized, involved in

common biological pathways, or connected *via* physical and genetic interactions. We listed the genes of interest in the ESI† and input the list into GeneMANIA. The tool provided information on the common features of the genes if there is any with a *Q*-value lower than 0.1, which was computed by the hypergeometric test with the Benjamini–Hochberg correction. Additional information is presented in the Results and discussion.

Statistical analysis

Host genomic sites harboring the integrated retroviral genomes were classified based on their genetic features using the QuickMap tool; genes, transcriptional start sites (TSSs), CpG islands, regulatory domains, and repetitive elements (Table 1). The frequencies of retroviral integrations into the featured genomic domains varied depending on the curvature of the culturing substrate. In particular, statistical significance of the difference in integration frequencies for each type of featured domains between the bare glass and bead substrate cases was quantified by the chi-square test. For the quantification given a type of featured domains, the numbers of retroviral integrations into the sites within the domains and outside of the domains were considered.

Results and discussion

Infection of human cells grown on engineered nanobead monolayers

Silica nanobeads with diameters of 300, 600, and 1200 nm were first synthesized by catalytic hydrolysis of tetraethyl orthosilicate (TEOS). The silica beads were then placed on flat polydimethylsiloxane stamps (PDMS) and rubbed with PDMS slab repeatedly until the beads were assembled as a monolayer (Fig. 1b). Silica bead monolayers were then transferred to the PEI-coated glass substrate and the PEI coating was removed. Next, we cultured HEK 293T cells on the three different monolayers of silica nanobeads (300 nm, 600 nm, and 1200 nm in diameter) and flat bare glass as a control condition (Fig. 1c). The nanobeads and flat bare glass had the same chemical composition and were different only in physical morphology (curved *versus* flat). At 7 h post-growth on these nanostructured substrates, cells were infected with MLV, which is a representative retrovirus and has been often used for human gene therapy trials.²² The virus was engineered to harbor an eGFP-coding gene that made infected cells green¹² (Fig. 1c).

After 8 days, which provided sufficient time for viral entry and the following infection steps (Fig. 1a), the genomic DNA of the infected cells was isolated and the regions of the host genome that newly harbored the viral DNA were determined by NGS and downstream bioinformatics analysis¹⁹ (Fig. 2a). While common biological experiments use millions of cells, thousands of cells were used in our experiments because it was difficult to prepare large-sized substrates with well-arranged nanobeads that can support the growth of millions of cells. In addition, only a fraction of retroviral integration

Table 1 Frequencies of MLV integrations into the featured host genomic regions. The frequencies of viral integrations into each type of genomic region are shown in percentages. The frequencies for cells grown on the nanobeads that are statistically significantly different from those for cells grown on bare glass are highlighted in red (when P -value < 0.05). Statistical significance of the difference between the cases was quantified with P -values that were calculated by the chi-square test. The numbers of cell-virus genome junctions that were captured by molecular biology techniques and sequenced by NGS are shown (n). To determine whether the number of the junctions was sufficient to statistically confirm the integration pattern difference, the achieved power values given the significance level ($\alpha = 0.05$), the effect size and the sample size were also calculated using G*Power 3.1 and shown with the P -values. Mapping of the host DNA sequences within cell-virus genome junctions to the human genome was performed with the QuickMap tool¹⁹

Genomic regions	Random ($n = 1\,000\,000$) %	Bare ($n = 35$)		300 nm ($n = 66$)				600 nm ($n = 27$)				1200 nm ($n = 401$)			
		%	n	%	n	Power	P -value	%	n	Power	P -value	%	n	Power	P -value
Within genes	44.6	54.3	19	65.2	43	0.426	7.6×10^{-2}	66.7	18	0.252	2.0×10^{-1}	59.6	239	0.570	3.3×10^{-2}
Within 5 kb of the TSSs	10.4	40.0	14	62.1	41	0.956	2.4×10^{-4}	55.6	15	0.378	9.9×10^{-2}	62.3	250	1.000	6.6×10^{-20}
Within 5 kb of CpG islands	7.2	40.0	14	63.6	42	0.975	8.8×10^{-5}	51.9	14	0.242	2.1×10^{-1}	55.4	222	1.000	3.4×10^{-10}
Within 5 kb of the regulatory domains	13.8	34.3	12	90.9	60	1.000	3.3×10^{-22}	92.6	25	1.000	1.7×10^{-10}	65.6	263	1.000	8.2×10^{-40}
Cis-regulatory elements	6.9	22.9	8	62.1	41	1.000	3.0×10^{-14}	59.3	16	0.995	6.7×10^{-6}	48.6	195	1.000	1.0×10^{-34}
miRNA target sites	6.7	11.4	4	28.8	19	0.993	9.3×10^{-6}	33.3	9	0.947	3.5×10^{-4}	16.5	66	0.886	1.5×10^{-3}
Repeats	48.9	31.4	11	33.3	22	0.063	7.4×10^{-1}	33.3	9	0.055	8.3×10^{-1}	26.7	107	0.535	4.1×10^{-2}

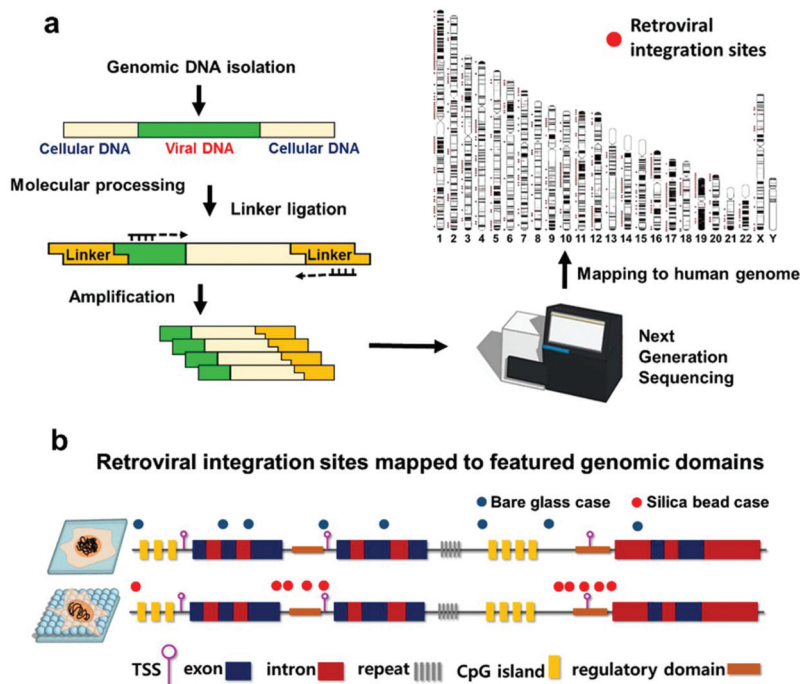


Fig. 2 Analysis of retroviral integrations. (a) Mapping of retroviral integrations to human genome. (b) Conceptual illustration of differences in retroviral integration patterns depending on the topography of cell culture substrates.

sites in infected cells can be captured even with current advances in NGS methods because identification of few integration sites in the large human genome of 3.2×10^9 bp is challenging and the efficiency of host-virus genome junction amplification is also limited. Owing to this technical limit-

ation, the numbers of integration sites detected in samples differed (Table 1). However, the whole analysis finally showed that retroviral DNA integration patterns can be significantly shifted due to interactions of human cells with nanostructured inorganic materials (Fig. 2b).

Retroviral genome integration patterns for cells on flat glass

MLV integrated into the host genomic regions within or near TSSs and CpG islands at the same frequency (40.0%) in human cells grown on bare glass (Table 1). CpG islands are the regions enriched in the CG sequence. In addition, MLV integrated into the regulatory domains at the frequency of 34.3% in cells grown on bare glass (Table 1). Among the regulatory domains, the cis-regulatory elements that control transcription of genes were more frequently selected by the virus than the miRNA target sites (22.9% and 11.4%, respectively, Table 1). The transcriptional products relevant to each miRNA target base-pair with the miRNAs and are finally degraded, which blocks translation of the transcripts. The retroviral integration frequencies for the above-mentioned genomic regions are considerably higher than the corresponding frequencies of computationally generated random integrations (3.8-fold higher for TSSs (P -value = 1.0×10^{-8}), 5.6-fold higher for CpG islands (P -value = 5.4×10^{-14}), and 2.5-fold higher for the regulatory domains (P -value = 4.3×10^{-4}), Table 1). This high preference for TSSs, CpG islands, and the regulatory domains is consistent with the MLV integration patterns observed in other studies.^{18,23–25}

Retroviral genome integration patterns for cells on nanobead layers

Compared to the frequencies for cells grown on bare glass, the frequencies of retroviral integrations into the TSS regions and CpG islands were increased by up to 56% and 59%, respectively (maximum frequencies were 62.3% for TSSs and 63.6% for CpG islands, Table 1) in cells grown on nanobeads. Remarkably, for cells grown on nanobeads, MLV integrated into the genomic regions that contained or were located near the regulatory domains at frequencies of up to 92.6%, which was 2.7-fold higher than that of cells grown on bare glass (34.3%, Table 1). The viral integration preference for the regulatory domains was equivalent in cells grown on the 300 nm and 600 nm bead layers (Table 1). This large difference in the integration frequencies for the regulatory regions between the bare glass and the nanobead cases cannot be easily observable by random chance (P -value = 3.3×10^{-22} for the 300 nm bead case and P -value = 1.7×10^{-10} for the 600 nm bead case). In addition, equivalent increases in the integration preference for the cis-regulatory elements (2.6- to 2.7-fold) and miRNA target sites (2.5- to 2.9-fold) were observed in cells grown on the 300 nm and 600 nm-beads. The increase in integration preference for the regulatory domains was less significant when cells were grown on the 1200 nm bead layer (65.6%, Table 1) compared to that of cells grown on bare glass.

Integration frequencies for the regulatory domains as a function of the curvature of culturing substrates

Viral integration preference for the regulatory domains was plotted against the curvature of the cell culture substrates (Fig. 3a). The integration frequency for the regulatory domains increased with the curvature. However, the integration fre-

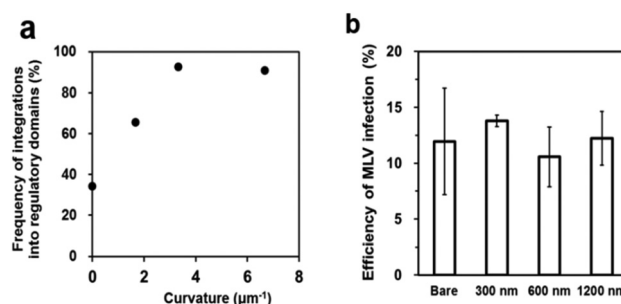


Fig. 3 Effects of the nanotopography of culturing substrates on retroviral infections. (a) Retroviral integration frequencies for the regulatory domains as a function of the curvature of culturing substrates. The 300 nm, 600 nm, and 1200 nm beads and bare glass have the curvatures of $6.67 \mu\text{m}^{-1}$, $3.33 \mu\text{m}^{-1}$, $1.67 \mu\text{m}^{-1}$, and $0.00 \mu\text{m}^{-1}$, respectively (calculated using the following formula: curvature = [nanobead radius] $^{-1}$). (b) Efficiency of MLV invasion into HEK 293T cells. Cells grown on the bare glass and nanobeads were infected with MLV that harbored the gene encoding eGFP. Infected cells were then quantified by counting eGFP-positive cells using flow cytometry 4 days post-addition of viruses into cells. Three independent infections and the subsequent quantifications were performed, and the standard deviations among the three independent measurements are shown as error bars.

quency for these genomic domains did not increase significantly beyond the curvature of $3.33 \mu\text{m}^{-1}$ (Fig. 3a). These significant changes in the retroviral integration frequencies for the featured genomic domains of cells grown on substrates with varying nanoscale curvature indicate, for the first time, that cellular responses to topographical cues from the environment can alter the responses to concurrent viral invasion.

Spatial distribution of retroviral integrations around featured genomic loci

We additionally evaluated the spatial distribution of the viral genome integrations in detail by quantifying the distance between integration spots and each featured host genomic region (Fig. 4a–d and S1 (ESI †)). First, while 25.7% of the MLV integrations were concentrated within 2 kb from TSSs when cells were grown on bare glass, the local integration frequencies for this TSS-proximal region were even higher for cells on the 300 nm, 600 nm, and 1200 nm bead layers (51.5%, 51.9%, and 43.6%, respectively, Fig. 4a). This spatially concentrated pattern of integrations into the TSS proximal region for the bead cases was more apparent when viral integration spots were marked on a wider window of the host genome (a window of 200 kb around TSSs, Fig. 4c). Second, MLV DNA integrations into the genomic regions of CpG islands and cis-regulatory elements were also concentrated around the centers of these featured genomic regions for cells grown on the nanobeads (Fig. S1a and S1b (ESI †) and Fig. 4b and d). For example, while 20.0% of the viral integrations were within the 2 kb window of cis-regulatory elements for cells grown on bare glass, 53.0%, 37.0%, and 40.9% of the integrations were within the same window for cells grown on the 300 nm, 600 nm, and 1200 nm bead layers, respectively (Fig. 4b and d). The regulatory

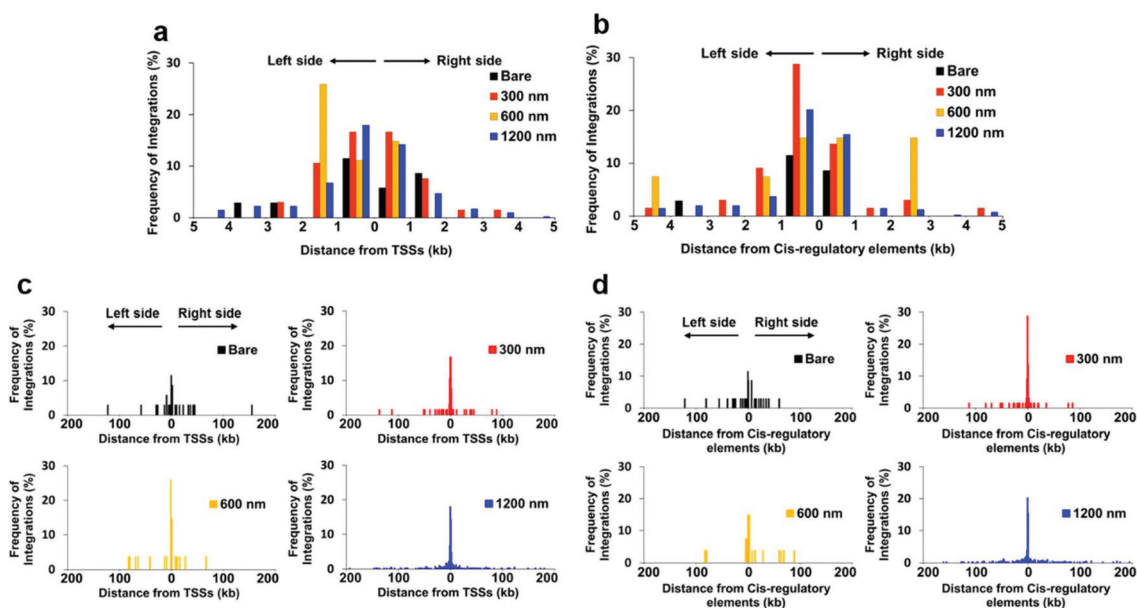


Fig. 4 Spatial distribution of MLV integrations around featured genomic loci. Spatial distribution of MLV integrations around TSSs (within a 5 kb window (a) and within a 200 kb window (c)). Spatial distribution of MLV integrations around cis-regulatory elements (within a 5 kb window (b) and within a 200 kb window (d)).

domains of human genome were sub-classified into cis-regulatory elements, miRNA target sites, and tissue-specific enhancers (Table 1).¹⁹ In contrast to the observation for cis-regulatory elements, highly concentrated viral integrations were not detected for the genomic regions around the miRNA target sites in cells grown on the bead layers, and only mild concentrations were observed (Fig. S1c and S1d†). The large increase in the MLV integration frequencies for TSSs, CpG islands, cis-regulatory elements, and miRNA target sites in the human genome (Table 1) should be caused by the way how HEK 293T cells sense and respond to the topography of nanostructured culturing substrates. Interestingly, MLV-infected cells grown on the curved nanostructures and cells on flat bare glass surface with similar efficiencies (Fig. 3b). Therefore, the question arises as to how the viral integration patterns are significantly shifted toward the regulatory genomic domains without any significant change in the success rate of the viral invasion of cells.

Retroviral integration sites as potential indicators showing the local states of the host genome

Previous studies have demonstrated that animal cells grown on nanostructures generated more and longer filopodia or microvilli and showed enhanced proliferation.^{26–29} These changes in cell morphology and growth were thought to be linked to variations in the topography of the culturing substrate. Recently, it was reported that the information on the topography of extracellular substrates can be transferred to the cell nuclei, and these cells ultimately alter their gene expression profiles, a phenomenon called mechanotransduction, *via* various changes, including physical reorientation of

their genomic DNA.^{30–34} For example, certain closed regions of genomic DNA can be opened by such external cues,^{30,32,33} allowing easier access for the transcription machinery. The whole or parts of some chromosomes can also relocalize within the internal territories of the nucleus.^{32,35,36} In addition, it is known that open genomic regions and euchromatin areas can be frequently hit by retroviral integrations.^{37,38} Therefore, we supposed that the list of the host genetic components or genes neighboring the integrated MLV genome may provide clues regarding which genomic regions are physically rearranged to be newly accessible while cells are responding to outer topographical signals. We mainly focused on the genomic domains near cis-regulatory elements because the frequency of MLV integrations was greatly increased for these domains in cells cultured on nanobeads (Table 1).

Functional mapping strategy for the genes of which spatially close cis-regulatory elements neighbored retroviral integration sites

We first listed all the genes of which spatially close cis-regulatory elements were located within 5 kb from MLV integration sites for all the cases of culturing substrates (Tables S1a–S1d). It has been suggested that the putative target genes of cis-regulatory elements are spatially closest to the elements.³⁹ If the listed genes for the bead cases commonly perform distinct cellular processes or functions unlike those for the bare glass case, it may indicate that the processes or functions can be activated *via* changes in the state of the genome regions harboring the corresponding genes when cells respond to the bead topography. During this functional analysis, the entire group of listed genes for each substrate case was named “Cis

group”, whereas a fraction of these genes, the TSSs of which were within 5 kb from the viral integration sites, was named “Cis-TSS group”. The other fraction of these genes of which spatially close cis-regulatory elements were within 5 kb from the viral integration sites but did not harbor TSSs within this genomic window was named “Cis-only group” (“Cis group” = “Cis-only group” + “Cis-TSS group”). We then attempted to discover the interactions among the genes or gene products and identify the specific biological functions of interactively connected subsets of the genes or gene products, if any, using a gene network construction tool, GeneMANIA.^{20,21} This systems biology tool identifies the connections among genes that users list, based on whether the genes are co-expressed, whether the gene products are co-localized, whether the genes or gene products genetically or physically interact with each other, and whether the gene products are involved in the same biological pathways.^{20,21} The chance of emergence of biological functions from these gene networks depends on whether the network is composed of genes relevant to this function and therefore may not positively correlate with the size of the network.

Genes associated with the low-curvature substrate cases

For the bare glass case (curvature = $0.00 \mu\text{m}^{-1}$), MLV integrated into cis-regulatory domains that were close to eight genes: *CDK13*, *AMD1*, *LCORL*, *SNX17*, *RMDN2*, *ADPRHL1*, *GNL3*, and *RPRM* (the “Cis group” for the bare glass case, Table S1a†). Among them, six genes, *CDK13*, *AMD1*, *LCORL*, *RMDN2*, *GNL3*, and *RPRM*, were connected as a genetic network based on their co-expression patterns (Fig. 5a). However, no common biological function was identified from this six-gene network.

Similarly, the “Cis-only group” for the bare glass case (Table S1a†) was not linked to any common biological function (not shown). In addition, the genetic networks for the “Cis group” and the “Cis-only group” of the 1200 nm (curvature = $1.67 \mu\text{m}^{-1}$) and 600 nm (curvature = $3.33 \mu\text{m}^{-1}$) bead cases (Tables S1b and S1c†) were not associated with any common biological function (Fig. 5b, c, S2a and S2b†).

Biological functions performed by genes associated with the highest-curvature substrate case

In stark contrast, the “Cis group” of the 300 nm bead case (the highest curvature case, Table S1d†) produced a genetic network, the subparts of which are associated with several common biological functions (Fig. 6a). GeneMANIA displays biological functions relevant to a genetic network when the genes in subparts of the parental network pass the Q-value cut-off of 0.1 for a certain functional category (please refer to the GeneMANIA server page; <http://pages.genemania.org/help>). The common biological functions detected for the “Cis group” of the 300 nm bead case include “chromatin”, “embryonic appendage morphogenesis”, “embryonic limb morphogenesis”, and others (Fig. 6a). Analysis of the “Cis-only group” of the 300 nm bead case revealed the top three biological functions (Fig. 6a) again (Fig. 6b), but with improved false discovery rates (FDR; ~ 0.05).

The five genes in the “Cis-only group” of the 300 nm bead case, *HDAC2*, *MCM2*, *RUVBL1*, *PSIP1* and *EXOSC4*, are involved in “chromatin” function (Fig. 6b). UniProt, a protein knowledge database, noted that the products of *RUVBL1* and *HDAC2* can modify local chromatin structures by changing the chemi-

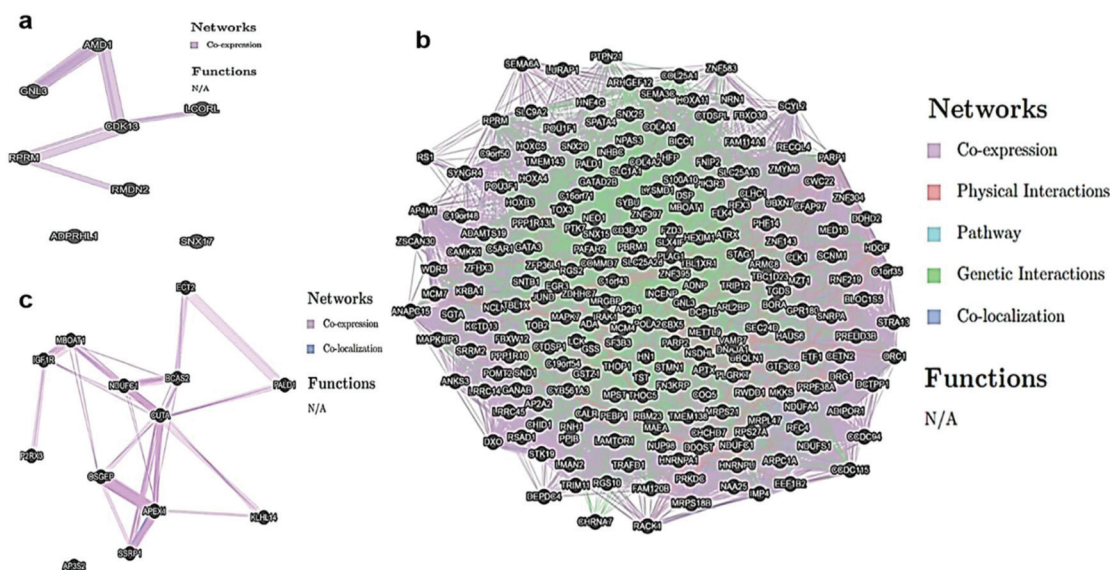


Fig. 5 Genetic networks and biological functions for the genes of which spatially close cis-regulatory elements are located within 5 kb from MLV integration sites. Genes shown as nodes are connected when the corresponding genes are related based on co-expression, co-localization, physical and genetic interactions between them, and involvement in common biological pathways.^{20,21} The nodes for specific genes that are involved in a common biological function are labeled with the corresponding color shown in the right box that lists the relevant functions. If a certain gene is involved in multiple biological functions, the gene node is filled with multiple colors corresponding to these functions. (a) For the “Cis group” of the bare glass case. (b) For the “Cis group” of the 1200 nm bead case. (c) For the “Cis group” of the 600 nm bead case.

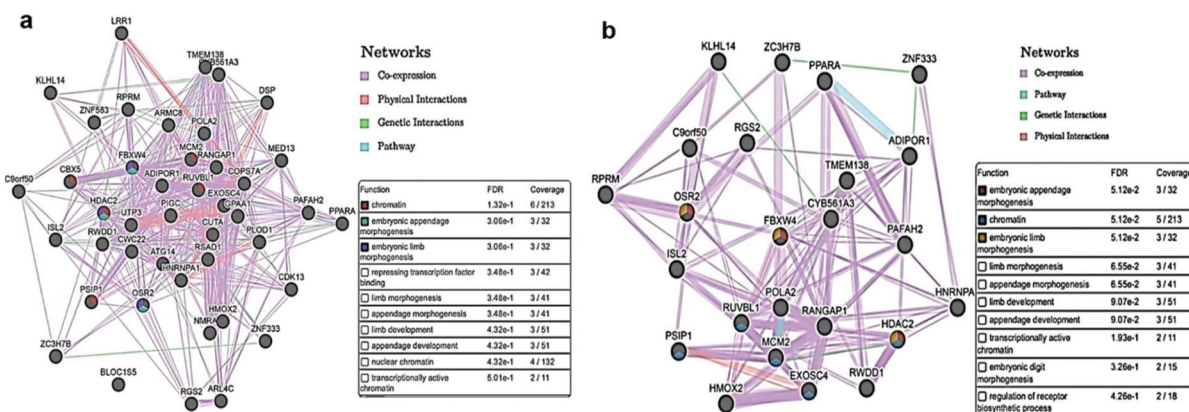


Fig. 6 Genetic networks and biological functions of genes, the spatially close cis-regulatory elements of which are located within 5 kb from MLV integration sites. (a) For the “Cis group” of the 300 nm bead case. (b) For the “Cis-only group” of the 300 nm bead case.

cal state of histones *via* acetylation and deacetylation.⁴⁰ Other gene products function as transcriptional activator (PSIP1) and a part of the replicative helicase (MCM2).⁴⁰ The product of *EXOSC4* is involved in histone mRNA degradation, which can possibly affect the chromatin structure as well. The concurrent MLV integrations observed near the regulatory genomic regions of multiple putative target genes that are involved in a common function relevant to “chromatin” indicate that these functional genomic domains might be rearranged to more easily harbor retroviral DNAs in cells cultured on high-curvature nanobeads (for the 300 nm bead case). A recent relevant study showed that cellular responses to micro-patterned sub-

strates can lead to changes in the chromatin state *via* alteration in the expression of chromatin-modifying components and the following histone modifications.⁴¹

However, the molecular mechanism underlying the transfer of topographical cues from the patterned substrate into the cell nuclei, resulting in gene expression alteration required for changes in the chromatin state, remains to be determined.⁴¹ For the “Cis-only group” of the 300 nm bead case, four additional biological functions were identified with an FDR less than 0.1: “limb morphogenesis”, “appendage morphogenesis”, “limb development”, and “appendage development” (Fig. S2c†). However, the mechanism by which the genes

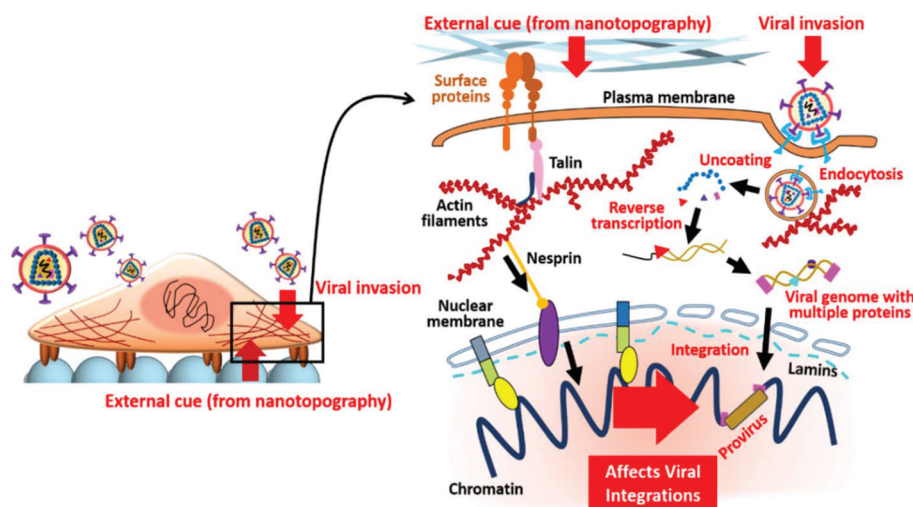


Fig. 7 Conceptual illustration of cellular responses to concurrent cues from nanotopography and invading viruses. Physical stimulus from extracellular environment is recognized by membrane surface proteins and generally transmitted along the cytoskeleton that spans the cytosol. The stimulus transmission can then be connected to the nucleus *via* linker of nucleoskeleton and cytoskeleton (LINC) complex formed by proteins located at nuclear membrane such as nesprins and SUN proteins. Finally, the stimulus can reach the chromatin *via* proteins tethering the chromatin with the nuclear lamins and induce changes in the structure of nuclear chromatin.^{57,58} On the other hand, a virus is internalized into the cytosol *via* endocytic pathways and the uncoated viral genome is converted into the double-stranded DNA by the viral reverse transcriptase. The resultant viral DNA forms pre-integration complex with multiple proteins to enter the nucleus. As the viral DNA integration site is determined by various factors, including proteins involved in formation of pre-integration complex and chromatin structure, the environmental cue may ultimately induce alterations in the viral integration sites.

related to body morphogenesis affected cellular morphology and sub-cellular functions in our experimental set-up is still unclear.

Interestingly, the products of three genes, *PSIP1*, *HDAC2* and *EXOSC4*, are also involved in interactions between host cells and viruses.⁴⁰ Lens epithelium-derived growth factor (LEDGF), the product of *PSIP1*, is a key host factor that determines HIV-1 (a lentivirus, widely grouped in retrovirus) integration patterns.^{42,43} *HDAC2* is linked to deacetylation of core histones, which often affects lentiviral transcription and latency.^{44–46} The product of *EXOSC4* provides cellular defense response to viral infection, reducing the cytopathic effects and viral titers.^{40,47}

Conclusions

Artificial substrates have long been used for culturing animal cells.^{48–50} Similar to natural environments, cells respond to these unnatural environments, albeit in different ways. Recent reports show that the mechanism by which cells respond to sophisticatedly designed surfaces of biocompatible materials can assist in controlling and engineering the function, physiology, and fate of cells.^{41,51–56} In this study, we showed for the first time that the mechanism by which human cells respond to nanostructured substrates can significantly affect the way these cells react to concurrently invading viruses (Fig. 7).

The cellular responses would be preceded by cellular sensing of the substrates, which often involves binding of the cell surface receptors, including various integrins, to the substrates. In particular, integrin binding to nanomaterials subsequently leads to the formation of focal adhesion where extracellular components, plasma membrane-associated molecules, and intracellular cytoskeletal proteins interact with each other. At the sites of focal adhesion, mechanical and biochemical information from the substrate environment starts to be transferred to the cell nucleus *via* signal transduction cascade and cytoskeletal reorganization.

After arriving at the nucleus, the outer information is further transmitted into the nucleus *via* LINC complex across the nuclear membrane.⁵⁹ Subsequently, heterochromatin protein 1 (HP1) and barrier-to-autointegration factor (BAF) can newly tether the nuclear lamina located in the peripheral region of the nucleus to different regions of chromatin.⁶⁰ This alteration in the arrangement of nuclear DNA possibly explains the observed changes in retroviral integration patterns (Fig. 7).

Existing viruses threaten human health; in addition, new or mutated viruses are continually emerging, including Ebola virus, Middle East respiratory syndrome coronavirus (MERS-CoV), and Zika virus.^{61,62} In contrast, several groups of viruses are being favorably utilized in gene and cell therapies after genetic engineering.^{9,22} To successfully treat virally infected patients, prevent viral infections, and advance virus-based therapeutics, effective tuning of the cell–virus interactions is required. This is the first study demonstrating that

engineered cell-culture substrate topography can alter host–virus interactions. Novel physical approaches based on engineered materials with various combinations of roughness, elasticity, and topography will be added to the existing chemical and biological approaches for controlling viral events. For example, virus-based gene delivery vectors cannot effectively transduce certain types of cells because of inefficient entry into the cells. Nanoengineering of cell culture substrates may enhance viral entry by triggering reorganization of cytoskeletal structures. In addition, the nanotopography-induced retroviral integration patterns that are highly concentrated in the regulatory genomic domains may facilitate genetic studies by allowing efficient system-wide perturbation of gene regulatory domains in the genome context and investigation of its effects on cellular phenotype.

Conflicts of interest

There are no conflicts to declare.

Acknowledgements

This research was supported by the National Research Foundation of Korea (NRF) funded by the Ministry of Science, ICT & Future Planning (2012M3A9B6055200). This research was supported by the Basic Science Research Program through the National Research Foundation of Korea (NRF) funded by the Ministry of Education (NRF-2015R1D1A1A01057099). This work was also supported by a grant from the National Research Foundation of Korea (NRF-2016M3A9B6947831).

Notes and references

- 1 D. E. Discher, D. J. Mooney and P. W. Zandstra, *Science*, 2009, **324**, 1673–1677.
- 2 D. E. Ingber, *Cell*, 1993, **75**, 1249–1252.
- 3 P. A. Janmey and C. A. McCulloch, *Annu. Rev. Biomed. Eng.*, 2007, **9**, 1–34.
- 4 V. Vogel and M. Sheetz, *Nat. Rev. Mol. Cell. Biol.*, 2006, **7**, 265–275.
- 5 D. Lingwood and K. Simons, *Science*, 2010, **327**, 46–50.
- 6 C. D. Roskelley, P. Y. Desprez and M. J. Bissell, *Proc. Natl. Acad. Sci. U. S. A.*, 1994, **91**, 12378–12382.
- 7 F. Y. McWhorter, T. Wang, P. Nguyen, T. Chung and W. F. Liu, *Proc. Natl. Acad. Sci. U. S. A.*, 2013, **110**, 17253–17258.
- 8 P. M. Mendes, *Chem. Soc. Rev.*, 2013, **42**, 9207–9218.
- 9 D. V. Schaffer, J. T. Koerber and K. I. Lim, *Annu. Rev. Biomed. Eng.*, 2008, **10**, 169–194.
- 10 M. Stahlhut, A. Schwarzer, M. Eder, M. Yang, Z. Li, M. Morgan, A. Schambach and O. S. Kustikova, *Biomaterials*, 2015, **63**, 189–201.
- 11 D. T. Wu and M. J. Roth, *Biomaterials*, 2014, **35**, 8416–8426.

- 12 J. M. Ignowski and D. V. Schaffer, *Biotechnol. Bioeng.*, 2004, **86**, 827–834.
- 13 J. Demeulemeester, S. Vets, R. Schrijvers, P. Madlala, M. De Maeyer, J. De Rijck, T. Ndung'u, Z. Debyser and R. Gijssbers, *Cell Host Microbe*, 2014, **16**, 651–662.
- 14 D. Derse, B. Crise, Y. Li, G. Princler, N. Lum, C. Stewart, C. F. McGrath, S. H. Hughes, D. J. Munroe and X. Wu, *J. Virol.*, 2007, **81**, 6731–6741.
- 15 F. B. Hashemi, K. Barreto, W. Bernhard, P. Hashemi, A. Lomness and I. Sadowski, *J. Virol.*, 2016, **90**, 5302–5314.
- 16 A. Moiani, Y. Paleari, D. Sartori, R. Mezzadra, A. Miccio, C. Cattoglio, F. Cocchiarella, M. R. Lidonnici, G. Ferrari and F. Mavilio, *J. Clin. Invest.*, 2012, **122**, 1653–1666.
- 17 L. S. Vranckx, J. Demeulemeester, Z. Debyser and R. Gijssbers, *PLoS One*, 2016, **11**, e0164167.
- 18 X. Wu, Y. Li, B. Crise and S. M. Burgess, *Science*, 2003, **300**, 1749–1751.
- 19 J. U. Appelt, F. A. Giordano, M. Ecker, I. Roeder, N. Grund, A. Hotz-Wagenblatt, G. Opelz, W. J. Zeller, H. Allgayer, S. Fruehauf and S. Laufs, *Gene Ther.*, 2009, **16**, 885–893.
- 20 D. Warde-Farley, S. L. Donaldson, O. Comes, K. Zuberi, R. Badrawi, P. Chao, M. Franz, C. Grouios, F. Kazi, C. T. Lopes, A. Maitland, S. Mostafavi, J. Montojo, Q. Shao, G. Wright, G. D. Bader and Q. Morris, *Nucleic Acids Res.*, 2010, **38**, W214–W220.
- 21 K. Zuberi, M. Franz, H. Rodriguez, J. Montojo, C. T. Lopes, G. D. Bader and Q. Morris, *Nucleic Acids Res.*, 2013, **41**, W115–W122.
- 22 S. L. Ginn, I. E. Alexander, M. L. Edelstein, M. R. Abedi and J. Wixon, *J. Gene Med.*, 2013, **15**, 65–77.
- 23 K. I. Lim, *Mol. Cells*, 2012, **33**, 525–531.
- 24 C. Cattoglio, D. Pellin, E. Rizzi, G. Maruggi, G. Corti, F. Miselli, D. Sartori, A. Guffanti, C. Di Serio, A. Ambrosi, G. De Bellis and F. Mavilio, *Blood*, 2010, **116**, 5507–5517.
- 25 T. Tsukahara, H. Agawa, S. Matsumoto, M. Matsuda, S. Ueno, Y. Yamashita, K. Yamada, N. Tanaka, K. Kojima and T. Takeshita, *Biochem. Biophys. Res. Commun.*, 2006, **345**, 1099–1107.
- 26 R. Muhammad, G. S. Peh, K. Adnan, J. B. Law, J. S. Mehta and E. K. Yim, *Acta Biomater.*, 2015, **19**, 138–148.
- 27 C. J. Bettinger, R. Langer and J. T. Borenstein, *Angew. Chem., Int. Ed.*, 2009, **48**, 5406–5415.
- 28 Y. H. Jang, S. Y. Yoon, Y. H. Cho, D. Lee, J. S. Lee and K. I. Lim, *Bull. Korean Chem. Soc.*, 2016, **37**, 1371–1373.
- 29 K. Kang, S. Y. Yoon, S. E. Choi, M. H. Kim, M. Park, Y. Nam, J. S. Lee and I. S. Choi, *Angew. Chem., Int. Ed.*, 2014, **53**, 6075–6079.
- 30 N. Wang, J. D. Tytell and D. E. Ingber, *Nat. Rev. Mol. Cell Biol.*, 2009, **10**, 75–82.
- 31 M. J. Dalby, N. Gadegaard, P. Herzyk, D. Sutherland, H. Agheli, C. D. Wilkinson and A. S. Curtis, *J. Cell. Biochem.*, 2007, **102**, 1234–1244.
- 32 P. M. Tsimbouri, K. Murawski, G. Hamilton, P. Herzyk, R. O. Oreffo, N. Gadegaard and M. J. Dalby, *Biomaterials*, 2013, **34**, 2177–2184.
- 33 C. Uhler and G. V. Shivashankar, *Nat. Rev. Mol. Cell Biol.*, 2017, **18**, 717–727.
- 34 K. J. Chalut, K. Kulangara, M. G. Giacomelli, A. Wax and K. W. Leong, *Soft Matter*, 2010, **6**, 1675–1681.
- 35 M. J. Dalby, M. O. Riehle, D. S. Sutherland, H. Agheli and A. S. Curtis, *Eur. J. Cell Biol.*, 2004, **83**, 159–169.
- 36 F. Bushman, M. Lewinski, A. Ciuffi, S. Barr, J. Leipzig, S. Hannenhalli and C. Hoffmann, *Nat. Rev. Microbiol.*, 2005, **3**, 848–858.
- 37 J. Demeulemeester, J. De Rijck, R. Gijssbers and Z. Debyser, *Bioessays*, 2015, **37**, 1202–1214.
- 38 E. Serrao and A. N. Engelman, *Crit. Rev. Biochem. Mol. Biol.*, 2016, **51**, 26–42.
- 39 R. Worsley-Hunt, V. Bernard and W. W. Wasserman, *Genome Med.*, 2011, **3**, 65.
- 40 C. The UniProt, *Nucleic Acids Res.*, 2017, **45**, D158–D169.
- 41 T. L. Downing, J. Soto, C. Morez, T. Houssin, A. Fritz, F. Yuan, J. Chu, S. Patel, D. V. Schaffer and S. Li, *Nat. Mater.*, 2013, **12**, 1154–1162.
- 42 A. Ciuffi, M. Llano, E. Poeschla, C. Hoffmann, J. Leipzig, P. Shinn, J. R. Ecker and F. Bushman, *Nat. Med.*, 2005, **11**, 1287–1289.
- 43 M. Llano, D. T. Saenz, A. Meehan, P. Wongthida, M. Peretz, W. H. Walker, W. Teo and E. M. Poeschla, *Science*, 2006, **314**, 461–464.
- 44 K. M. Barton, N. M. Archin, K. S. Keedy, A. S. Espeseth, Y. L. Zhang, J. Gale, F. F. Wagner, E. B. Holson and D. M. Margolis, *PLoS One*, 2014, **9**, e102684.
- 45 S. E. Kauder, A. Bosque, A. Lindqvist, V. Planelles and E. Verdin, *PLoS Pathog.*, 2009, **5**, e1000495.
- 46 C. Van Lint, S. Bouchat and A. Marcello, *Retrovirology*, 2013, **10**, 67.
- 47 M. Miyashita, H. Oshiumi, M. Matsumoto and T. Seya, *Mol. Cell. Biol.*, 2011, **31**, 3802–3819.
- 48 V. Ruprecht, P. Monzo, A. Ravasio, Z. Yue, E. Makhija, P. O. Strale, N. Gauthier, G. V. Shivashankar, V. Studer, C. Albiges-Rizo and V. Viasnoff, *J. Cell Sci.*, 2017, **130**, 51–61.
- 49 D. E. Discher, P. Janmey and Y. L. Wang, *Science*, 2005, **310**, 1139–1143.
- 50 A. Khademhosseini, R. Langer, J. Borenstein and J. P. Vacanti, *Proc. Natl. Acad. Sci. U. S. A.*, 2006, **103**, 2480–2487.
- 51 W. L. Murphy, T. C. McDevitt and A. J. Engler, *Nat. Mater.*, 2014, **13**, 547–557.
- 52 M. Ventre and P. A. Netti, *ACS Appl. Mater. Interfaces*, 2016, **8**, 14896–14908.
- 53 K. Yang, H. Jung, H. R. Lee, J. S. Lee, S. R. Kim, K. Y. Song, E. Cheong, J. Bang, S. G. Im and S. W. Cho, *ACS Nano*, 2014, **8**, 7809–7822.
- 54 M. P. Lutolf, P. M. Gilbert and H. M. Blau, *Nature*, 2009, **462**, 433–441.
- 55 L. E. McNamara, R. Burchmore, M. O. Riehle, P. Herzyk, M. J. Biggs, C. D. Wilkinson, A. S. Curtis and M. J. Dalby, *Biomaterials*, 2012, **33**, 2835–2847.
- 56 F. Morena, I. Armentano, P. Montanucci, C. Argentati, E. Fortunati, S. Montesano, I. Bicchi, T. Pescara,

- I. Pennoni, S. Mattioli, L. Torre, L. Latterini, C. Emiliani, G. Basta, R. Calafiore, J. M. Kenny and S. Martino, *Biomaterials*, 2017, **144**, 211–229.
- 57 M. L. Lombardi, D. E. Jaalouk, C. M. Shanahan, B. Burke, K. J. Roux and J. Lammerding, *J. Biol. Chem.*, 2011, **286**, 26743–26753.
- 58 A. Tajik, Y. Zhang, F. Wei, J. Sun, Q. Jia, W. Zhou, R. Singh, N. Khanna, A. S. Belmont and N. Wang, *Nat. Mater.*, 2016, **15**, 1287–1296.
- 59 N. Wang, *J. Phys. D: Appl. Phys.*, 2017, **50**, 233002.
- 60 M. Loi, V. Cenni, S. Duchi, S. Squarzone, C. Lopez-Otin, R. Foisner, G. Lattanzi and C. Capanni, *Oncotarget*, 2016, **7**, 15662–15677.
- 61 J. Mlakar, M. Korva, N. Tul, M. Popovic, M. Poljsak-Prijatelj, J. Mraz, M. Kolenc, K. Resman Rus, T. Vesnaver Vipotnik, V. Fabjan Vodusek, A. Vizjak, J. Pizem, M. Petrovec and T. Avsic Zupanc, *N. Engl. J. Med.*, 2016, **374**, 951–958.
- 62 K. Kupferschmidt, *Science*, 2015, **347**, 1296–1297.